

Swarm behavior of self-propelled rods and swimming flagella

Yingzi Yang,¹ Vincent Marceau,^{1,2} and Gerhard Gompper¹

¹Theoretical Soft Matter and Biophysics Group, Institut für Festkörperforschung, Forschungszentrum Jülich, D-52425 Jülich, Germany

²Département de physique, de génie physique et d'optique, Université Laval, Québec, Québec, Canada G1V 0A6

(Dated: October 31, 2018)

Systems of self-propelled particles are known for their tendency to aggregate and to display swarm behavior. We investigate two model systems, self-propelled rods interacting via volume exclusion, and sinusoidally-beating flagella embedded in a fluid with hydrodynamic interactions. In the flagella system, beating frequencies are Gaussian distributed with a non-zero average. These systems are studied by Brownian-dynamics simulations and by mesoscale hydrodynamics simulations, respectively. The clustering behavior is analyzed as the particle density and the environmental or internal noise are varied. By distinguishing three types of cluster-size probability density functions, we obtain a phase diagram of different swarm behaviors. The properties of clusters, such as their configuration, lifetime and average size are analyzed. We find that the swarm behavior of the two systems, characterized by several effective power laws, is very similar. However, a more careful analysis reveals several differences. Clusters of self-propelled rods form due to partially blocked forward motion, and are therefore typically wedge-shaped. At higher rod density and low noise, a giant mobile cluster appears, in which most rods are mostly oriented towards the center. In contrast, flagella become hydrodynamically synchronized and attract each other; their clusters are therefore more elongated. Furthermore, the lifetime of flagella clusters decays more quickly with cluster size than of rod clusters.

I. INTRODUCTION

Systems of self-propelled particles (SPP), which exhibit an interaction mechanism that favors velocity alignment of neighboring particles, often display collective behaviors like swarming and clustering. There are many examples for this swarming behavior, ranging from systems of microscopic particles (sperm, bacteria, nano-rods) to systems of macroscopic objects (birds, fish).

Since the pioneering simulation work of Vicsek et al. [1], SPP systems have attracted a lot of interest at the theoretical [2–8] and computational [9–15] level. Typically, in simulation models of swarm behavior, point-like agents move with an imposed non-zero velocity and tend to align their direction of motion with others in a prescribed neighborhood [1, 10, 11, 14]. Although the alignment mechanism may differ from one model to the other, the basic properties of swarm behavior are quite universal [16]. Upon variation of parameters such as particle density, particle velocity, or environmental noise, the system can undergo a transition from a disordered state, where the average total velocity or orientation vanishes, to a nematic-like ordered state. Near the transition point, the cluster-size probability density function is characterized by a power-law decay [11, 16]. For intermediate densities, phase separation into regions of different density and band formation has been found [15].

Self-propelled motion is common in biological systems at micro- or mesoscopic length scales, such as suspensions of bacteria, like *E. coli* [17] and *Bacillus subtilis* [18–20], or tissue cells (keratocytes) [9], whose sizes are all on the micrometers scale. A special class of biological systems are rod-like self-propelled particles (rSPP), for example myxobacteria (approximately $10\mu\text{m}$ long) [21, 22]. When starved, myxobacteria are elongated to an average aspect ratio of approximately 1:7, glide on a substrate along their long axis and undergo a process of alignment, rippling, streaming and aggregation that culminates in a three-dimensional fruiting body. A model,

which takes into account the exchange of a morphogen during cell-cell contact and a preferred cell motion in the direction of largest morphogen concentration, has been designed to describe the streaming and two-stage aggregation of myxobacteria [23].

Sperm (with a length of about $50\mu\text{m}$) [24, 25] and nematodes [26] (about 1mm long) employ a sinusoidal undulation of their slender bodies to push the fluid backwards and to propel themselves forward. Large train-like clusters of wood mouse sperm [27, 28] are believed to result in greater thrust forces to move more efficiently through a highly viscous environment. The wood mouse sperm has a hook-like structure at its head, by which it can be hitched to the mid-part or the tail of a neighboring cell for robust cooperation. However, nematodes which do not have hook structures, also display a pronounced tendency to adhere to each other in a film of water, to form assemblies consisting of many organisms, and to exhibit a striking co-ordinated movement [26]. Also, sea urchin sperm organize into a hexagonal pattern of rotating vortices at surfaces [29].

A nice physical realization of self-propelled rods (SPR) are bimetallic nano-rods consisting of long Pt and Au segments [30]. The rods, about 300nm in diameter and $2\mu\text{m}$ long, move autonomously in an aqueous hydrogen peroxide solutions by catalyzing the formation of oxygen at the Pt end. They move predominantly in the direction of the Pt end, with a velocity depending on the concentration of hydrogen peroxide. When a gradient of the hydrogen peroxide concentration is imposed, the rods exhibit directed motion towards regions of higher concentrations through active diffusion [31].

A related system is a fluidized monolayer of macroscopic rods in the nematic liquid crystalline phase [32]. The rods confined between two hard walls are energized by an external vertical vibration, and gain kinetic energy through frequent collisions with the floor and the ceiling of the container. Long-lived giant number fluctuations are found, which shows that simple contact can give rise to flocking, coherent swirling

motion and large-scale inhomogeneities [33]. However, in this experiment, the rods do not have a preferred direction of motion.

All of these examples of self-propelled particles employ different propulsion mechanisms and have different interactions. However, their swarm behavior, such as flocking, streaming and clustering, is surprisingly similar. The common characteristic of these systems is their rod-like structures and their quasi-two-dimensional active motion. Myxobacteria glide on surfaces [21], while sperm and nematodes gather at substrates [26, 29, 34]. In suspensions of rod-like particles in thermal equilibrium, volume exclusion favors the alignment of rods. At high densities, it stabilizes a nematic state characterized by long-range orientational order [35].

While constant-velocity polar point particles interacting locally by nematic alignment in the presence of noise have been studied intensively in recent years [1–15], much less is known theoretically about the behavior of elongated particles with volume exclusion, or about the collective behavior of swimmers with hydrodynamic interactions. Previous simulation studies of self-propelled rods (SPR) in two dimensions show that self-propelled motion enhances the tendency for nematic ordering [36], as well as aggregation and clustering [37]. Also, rods have an increased probability to be located near surfaces (depending on their velocity, length and thermal noise) [38] and form hedgehog-like clusters at surfaces [39]. In Ref. [37], two regimes of clustering have been distinguished by their unimodal or bimodal weighted cluster-size distribution functions; however, the system contained a relatively small number of particles compared to those employed in simulation studies of swarming of SPPs. Continuum equations for the description of SPR systems have been derived recently within a mean-field approximation [6, 7]. This theory predicts that hard-core interactions are insufficient to generate a macroscopically polarized state, because they cannot distinguish the two ends of a rod, and makes interesting predictions for the fluctuations in the nematic and isotropic state (such as a crossover from diffusive to propagating density fluctuations). However, the mean-field approximation of volume exclusion has the limitation of omitting correlation effects, and thus works best for slowly varying density distributions.

In addition, hydrodynamic interactions between rSPP have so far been largely neglected. These interactions depend on the type of self-propulsion, where “pullers” repel and “pushers” attract each other [40, 41]. Nematic suspensions of swimming rod-like pushers are found to be unstable at long wavelengths as a result of hydrodynamic fluctuations [42]. For sperm and flagella, it has been shown theoretically that the hydrodynamic coupling synchronizes the phases of their sinusoidal beating tails [24, 43, 44]. Also, the hydrodynamic interaction between these microswimmers implies attraction and cluster formation [43]; similarly, it makes an essential contribution to the capturing of sperm near walls [45]. However, the relative importance of directed self-propulsion, particle shape, volume exclusion, and hydrodynamic interactions to the emergence of swarm behavior remains unclear.

In this paper, we employ a model of hard rods with strict volume exclusions and simulate large systems containing at

least 1000 particles. We focus on rSPP systems at a density below the isotropic-nematic transition of Brownian rods. We employ a model consisting of rigid SPR performing an overdamped translational motion in two dimensions, and analyze the resulting cluster-size probability density distribution, cluster configurations and lifetimes. Three types of cluster-size probability density distribution functions allow to distinguish three different states, and to construct a phase diagram as a function of particle density and environmental noise. As a special case of rSPP with an explicit propulsion mechanism, we investigate a suspension of flagella, which move by sinusoidal beating of their body in a two-dimensional fluid. The motion of the surrounding fluid is described by particle-based mesoscopic simulation method called multi-particle collision dynamics (MPC) [46, 47]. This method has been shown to capture the full hydrodynamics and flow behavior of complex fluids over a wide range of Reynolds numbers very well [48]. By comparing the results for SPR and flagella, we elucidate the contribution of hydrodynamic interactions to the swarm behavior.

This paper is organized as follows. Section II gives a brief description of our models and simulation methods. We analyze the collective behavior of SPR systems in Sec. III. In Sec. IV, we study the swarm behavior of flagella, and compare the results obtained with both models. The influence of hydrodynamic interactions and the flagellar beat on the swarm behavior are discussed. We summarize our main conclusions in Sec. V.

II. MODELS AND SIMULATION TECHNIQUES

A. Self-Propelled Rods

We consider a system of N_{rod} rods of length L_{rod} in a two-dimensional simulation box of size $L_x \times L_y$. Each rod is characterized by an orientation angle $\theta_{rod,i}$ with respect to the x -axis, a center-of-mass position $\mathbf{r}_{rod,i}$, a center-of-mass velocity $\mathbf{v}_{rod,i}$ and an angular velocity $\omega_{rod,i}$ around its center of mass (see Fig. 1a). The rods move ballistically according to their velocities,

$$\mathbf{r}_{rod,i}(t + \Delta t_{rod}) = \mathbf{r}_{rod,i}(t) + \mathbf{v}_{rod,i}(t)\Delta t_{rod}, \quad (1)$$

$$\theta_{rod,i}(t + \Delta t_{rod}) = \theta_{rod,i}(t) + \omega_{rod,i}(t)\Delta t_{rod}, \quad (2)$$

where Δt_{rod} is the simulation time step. The particle velocity can be decomposed into a parallel and a perpendicular component relative to the rod axis, $\mathbf{v}_{rod,i} = \mathbf{v}_{rod,i,\parallel} + \mathbf{v}_{rod,i,\perp}$.

We consider the rods to be embedded in an overdamped fluid medium where hydrodynamics can be approximated by an anisotropic friction on the rod-like particles. The motion is then determined by

$$\mathbf{v}_{rod,i,\parallel}(t) = \frac{1}{\gamma_{\parallel}} \left(\sum_{j \neq i}^{N_{rod}} \mathbf{F}_{ij,\parallel} + \xi_{\parallel} \mathbf{e}_{\parallel} + F_{rod,0} \mathbf{e}_{\parallel} \right), \quad (3)$$

$$\mathbf{v}_{rod,i,\perp}(t) = \frac{1}{\gamma_{\perp}} \left(\sum_{j \neq i}^{N_{rod}} \mathbf{F}_{ij,\perp} + \xi_{\perp} \mathbf{e}_{\perp} \right), \quad (4)$$

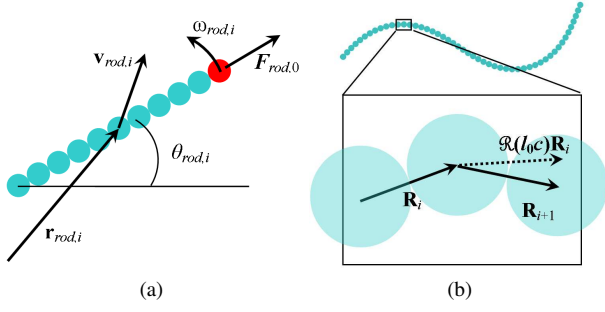


FIG. 1: (Color online) (a) Model of a self-propelled rod, and the coordinates used in two dimensions. The rod is discretized into $n_{rod} = L_{rod}/l_b$ beads for the calculation the volume-exclusion interaction. (b) Model of a flagellum in two dimensions.

$$\omega_{rod,i}(t) = \frac{1}{\gamma_r} \left(\sum_{j \neq i}^{N_{rod}} M_{ij} + \xi_r \right), \quad (5)$$

where \mathbf{e}_{\parallel} and \mathbf{e}_{\perp} are the local parallel and perpendicular unit vectors of the rod orientation. $F_{rod,0}$ is a constant propelling force applied along \mathbf{e}_{\parallel} . The friction coefficients are given by $\gamma_{\perp} = 2\gamma_{\parallel}$, $\gamma_{\parallel} = L_{rod}$ and $\gamma_r = \gamma_{\parallel} L_{rod}^2/6$. The random forces ξ_{\parallel} , ξ_{\perp} and ξ_r are white noises, which are determined by their variances $\sigma_{rod}^2 L_{rod}$, $\sigma_{rod}^2 L_{rod}$ and $\sigma_{rod}^2 L_{rod}^3/12$, respectively. Finally, \mathbf{F}_{ij} is the force generated by volume exclusion between rods i and j , and M_{ij} is the torque generated by \mathbf{F}_{ij} on rod i in the reference system of center of mass of rod i .

For the calculation of the interactions, each rod is discretized into $n_{rod} = L_{rod}/l_b$ beads of diameter l_b , as illustrated in Fig. 1a. The volume exclusion between rods is then modelled by a shifted and truncated Lennard-Jones potential

$$V(r) = \begin{cases} 4\epsilon \left[\left(\frac{l_b}{r} \right)^{12} - \left(\frac{l_b}{r} \right)^6 \right] + \epsilon, & r < 2^{1/6} l_b \\ 0, & r \geq 2^{1/6} l_b \end{cases}, \quad (6)$$

between beads belonging to different rods, where r is the distance between two beads, l_b is the bead diameter, and ϵ is the strength of the potential. We use ϵ as the energy scale in our SPR simulations.

A single rod without noise then moves with a constant velocity $v_0 = F_{rod,0}/\gamma_{\parallel}$. In the non-zero noise regime, the diffusion constant along the parallel direction is $D_{\parallel} = \sigma_{rod}^2 L_{rod} \Delta t_{rod} / 2\gamma_{\parallel}^2$. The dimensionless Péclet number, which measures the ratio of self-propelled and diffusive motion, is thus

$$\text{Pe} = \frac{L_{rod} v_0}{D_{\parallel}} = \frac{2\gamma_{\parallel} F_{rod,0}}{\sigma_{rod}^2 \Delta t_{rod}}. \quad (7)$$

We use $1/\text{Pe} \propto \sigma_{rod}^2$ to characterize the strength of the environmental noise.

In SPR systems [6, 37], alignment is naturally introduced by the volume exclusion between the anisotropic particles; this also implies that the interaction neighborhood needs no further assumptions, but is directly related to the rod length. Hard-core interactions do not distinguish the two ends of an

symmetrically elongated object. Thus, both parallel and anti-parallel velocity configurations are induced. In simulations of point-like SPPs, noise is implemented by adding a random component to the velocity *orientation* of each particle. In our model of SPR, random forces are applied on each rod, which results in fluctuations in both the magnitude and the orientation of the velocity vectors. For a single rod, the orientation fluctuations lead to rotational diffusion, which implies a persistence length

$$L_p = \frac{2v_0\gamma_{\parallel}^2}{\sigma_{rod}^2 L_{rod} \Delta t} \quad (8)$$

of its trajectory. Note that the noise forces are not caused by thermal fluctuations, which would require a factor two between the variance of the random forces in parallel and perpendicular directions. In most biological and synthetic rSPP systems, thermal fluctuations are indeed negligible due to large size of the particles. In these systems, the environmental noise arises, for example, from density fluctuations of signalling molecules for chemotactic swimmers, or from fluctuations of the motor activity.

We use rods of length $L_{rod} = 11l_b$ and undisturbed velocity $v_0 = 1.21\epsilon/(\gamma L_{rod})$. Effects of a polydispersity of rod lengths or a distribution of propulsion forces are not considered. The motion of rods are calculated with a discrete time step $\Delta t_{rod} = 0.001$. Most of our rod simulations start from random initial states, where the rods are placed into the simulation box with random orientations and random positions without overlap. If not explicitly mentioned, the size of the simulation box is $L_x = L_y = 400l_b$, which is much larger than the rod length. Periodic boundary conditions are employed.

Our model differs from the model of Ref. [37] by the type of repulsive interaction between the rods. In Ref. [37], rods interact by a ‘‘soft’’ volume exclusion, where the repulsion force is proportional to the square of overlapping area, while in our model the interaction is a short-range Lennard-Jones potential between discretized beads. In the limit of a large overlap energy, the two models become equivalent.

B. Flagella

We consider a system of N_{fl} flagella of length L_{fl} in a box of size $L_x \times L_y$. Each flagellum consists of semi-flexible string of monomers of mass m_{fl} , connected by springs (see Fig. 1b). The shape of the flagellum is determined by the elastic energy

$$E = \sum_i \frac{k}{2l_0^2} (|\mathbf{R}_i| - l_0)^2 + \sum_i \frac{\kappa}{2l_0^3} \left\{ \mathbf{R}_{i+1} - \mathcal{R}(l_0 c) \mathbf{R}_i \right\}^2 + V. \quad (9)$$

Here, the first term is the harmonic potential generated by springs with spring constant k and rest length l_0 . \mathbf{R}_i is the bond vector pointing from monomer i to monomer $(i+1)$. The second term of Eq. (9) is the bending energy the flagellum, with bending rigidity κ . $\mathcal{R}(l_0 c)$ is an operator which rotates a two-dimensional vector clockwise by an angle $l_0 c$. The local spontaneous curvature c varies with time t and position x along the flagellum to generate a propagating bending

wave,

$$c(x, t) = A \sin \left[-2\pi f t + q x + \varphi \right]. \quad (10)$$

The detailed analysis of the beating pattern of nematodes [26] and bull sperm [25, 49] has shown that a single sine mode represents the beating pattern to a good approximation. We use the wave number $q = 2\pi/L_{fl}$, such that the phase difference between the first and the last monomer is 2π and one complete wavelength is present on the flagellum. The beating frequency f is constant for each flagellum; it is chosen from a Gaussian distribution, centered at f_0 and with variance $\sigma_{fl}^2 f_0^2$. φ is the initial phase of the first monomer, which is chosen from a uniform distribution in $[0, 2\pi]$. As t increases, a wave propagates along the flagellum from the first to the last monomer, pushing the fluid backwards and propelling the flagellum forward. Although the spontaneous local curvature c is prescribed by Eq. (10), the flagellum is elastic and its configuration is affected by the viscosity of the medium and the flow field generated by other flagella. The third term in Eq. (9) describes the interaction between flagella due to volume exclusion; here, we employ again the shifted and truncated Lennard-Jones potential (Eq. (6)) between monomers of different flagella.

Our model of a flagellum differs from the model of a sperm employed in Ref. [43] by the absence of a passive midpiece and a circular head. Also, in the sperm simulations [43], two sine waves were present on the tail, while a single sine wave is present on the flagellum.

We use flagella of length $L_{fl} = 50l_0$. The elastic moduli in Eq. (9) are the spring constant $k = 1.25 \times 10^4 k_B T$ and the bending rigidity $\kappa = 200 k_B T L_{fl}$. The amplitude $A = 5/L_{fl}$ of the spontaneous curvature in Eq. (10) induces a beating amplitude of about $6.1 l_0 = 0.13 L_{fl}$. The strength $\epsilon = 15 k_B T$ of the volume exclusion is large compared to the thermal energy. The simulations are initialized by placing N_{fl} flagella in the simulation box with random initial positions and orientations, without any overlap. The size of the simulation box is $L_x \times L_y$, where $L_x = L_y = 400l_0$, eight times the length of a flagellum. Periodic boundary conditions are employed.

Each simulation run of the flagella systems covers a total time interval of about 3300 beats. The first 800 beats are not taken into account in the calculation of averages, in order to allow the system to reach the stationary state. This time is longer than the largest relaxation time of about 650 beats observed in the system with a width $\sigma_{fl} = 0.1\%$ of the frequency distribution.

C. Multi-Particle-Collision Dynamics (MPC)

MPC is a particle-based mesoscopic simulation technique used to describe the hydrodynamics and flow behavior of complex fluids. The fluid is modeled by N_{sol} point particles of mass $m_{sol,i}$, which are characterized by their continuous space position $\mathbf{r}_{sol,i}$ and velocity $\mathbf{v}_{sol,i}$. During every time step Δt_{MPC} , there are two distinct simulation steps, streaming and collision. In the streaming step, the fluid particles do not interact with each other and move ballistically according to their

velocities,

$$\mathbf{r}_{sol,i}(t + \Delta t_{MPC}) = \mathbf{r}_{sol,i}(t) + \mathbf{v}_{sol,i}(t) \Delta t_{MPC}. \quad (11)$$

In the collision step, the particles are sorted into the cells of a square lattice of side length a according to their position, and interact with all other particles in same collision box through a multi-body collision. The collision step is defined by a rotation of all particle velocities in a box in a co-moving frame with its center of mass. Thus, the velocity of the i -th particle in the j -th box after collision is

$$\mathbf{v}_{sol,i}(t + \Delta t_{MPC}) = \mathbf{v}_{cm,j}(t) + \mathfrak{R}_j(\alpha) [\mathbf{v}_{sol,i} - \mathbf{v}_{cm,j}] \quad (12)$$

where

$$\mathbf{v}_{cm,j}(t) = \frac{\sum_i m_{sol,i} \mathbf{v}_{sol,i}}{\sum_i m_{sol,i}} \quad (13)$$

is the center-of-mass velocity of j -th box, and $\mathfrak{R}_j(\alpha)$ is a rotation matrix which rotates a vector by an angle $\pm\alpha$, with the sign chosen at random. This implies that during the collisions particles exchange momentum, but the total momentum and kinetic energy are conserved within each collision box. In order to ensure Galilean invariance, a random shift of the collision grid has to be performed [50].

The total kinematic viscosity ν is the sum of two contributions, the kinetic viscosity ν_{kin} and the collision viscosity ν_{coll} . In two dimension, approximate analytical expressions are [51, 52],

$$\frac{\nu_{coll}}{\sqrt{k_B T a^2 / m_{sol}}} = \frac{1}{12h} (1 - \cos \alpha) \left(1 - \frac{1}{\rho} \right) \quad (14)$$

$$\frac{\nu_{kin}}{\sqrt{k_B T a^2 / m_{sol}}} = h \left[\frac{1}{1 - \cos \alpha} \frac{\rho}{\rho - 1} - \frac{1}{2} \right] \quad (15)$$

where ρ is the average particle number in each box and $h = \Delta t_{MPC} \sqrt{k_B T / m_{sol} a^2}$ is the rescaled mean free path. We use $k_B T = 1$, $m = 1$, $a = 1$, $\Delta t_{MPC} = 0.025$, $\alpha = \pi/2$, and $\rho = 10$. This implies, in particular, that the simulation time unit $(m a^2 / k_B T)^{1/2}$ equals unity. With these parameters, the total kinematic viscosity of fluid is $\nu = \nu_{coll} + \nu_{kin} \approx 3.02$.

During the MPC streaming step, the equations of motion of the flagella monomers are integrated using a velocity-Verlet algorithm, with a molecular-dynamics time step $\Delta t_{fl} = \Delta t_{MPC} / 50 = 5 \times 10^{-4}$. The bond length between the monomers is related to the collision cell size by $l_0 = a/2$. The flagella only interact with the fluid during the MPC collision step. This is done by sorting the flagella monomers together with the fluid particles into the collision cells and rotating their velocities relative to the center-of-mass velocity of each cell. Since energy is continuously injected into the system by the actively beating flagella, we employ a thermostat to keep the fluid temperature constant by rescaling all fluid-particle velocities in a collision box relative to its center-of-mass velocity after each collision step.

With the parameters given above, a single flagellum with $f_0 = 1/120$ swims forwards with the velocity $v_{single} = 0.020 \pm 0.001$ in a MPC fluid. Thus, we estimate a Reynolds number

	power law	rods	flagella
$\Pi(n)$	n^β	$-6 < \beta \approx -2$	$-4 < \beta \approx -2$
$\langle n \rangle$	Pe^ζ	$\zeta = 0.37$	
$\langle n \rangle$	$\sigma_{fl}^{-\zeta}$		$\zeta = 0.26$
T_{life}	$n^{-\delta}$	$\delta = 0.2$	$\delta = 0.5$

TABLE I: Definition of power-law exponents for the cluster size distribution $\Pi(n)$, the average cluster size $\langle n \rangle$, and the cluster lifetime T_{life} , and their typical values for rods and flagella.

$Re = 2A_{fl}v_{single}/\nu \approx 0.04$ for our flagellum model, where $A_{fl} = 0.12L_{fl}$ is the beating amplitude. The velocity of our flagella can be compared with the velocity of an *infinitely long* string beating in a two-dimensional fluid at $Re = 0$, which was calculated analytically by Taylor [24] to be

$$v_{single} = \frac{2\pi A_{fl}^2 v_{wave}}{\lambda_{wave}^2} \left(1 - \frac{19}{4} \frac{\pi^2 A_{fl}^2}{\lambda_{wave}^2} \right) \quad (16)$$

where λ_{wave} is the wave length and $v_{wave} = \lambda_{wave}f$ is the propagation velocity of the sinusoidal wave on the flagellum. Applying the parameters in our simulations, we obtain $v_{single} = 0.0183$, in excellent agreement with the simulation result. This demonstrates that the simulation model describes the limit of low-Reynolds-number hydrodynamics very well.

III. SWARMING BEHAVIOR OF SELF-PROPELLED RODS

After starting from a random initial state, the rods aggregate and form clusters. Large clusters can form by collisions of smaller ones, while at the same time they can break up due to collisions with other clusters or due to the noisy environment. After a transient phase, the system reaches a stationary state, in which the formation rate of any cluster size equals its break-up rate. The degree of aggregation in the system depends on its parameters such as the Péclet number and the number density $\rho_{rod} = N_{rod}/L_x L_y$.

We define a cluster as follows. We consider two rods to be in the same cluster if the angle between their orientation vectors is less than $\pi/6$ and the nearest distance is less than $2l_b$, which is about two times the width of a rod. A cluster is defined as a set of rods that are neighbors either directly or through other rods at a given moment in time. Its size is simply the number of rods it contains. A freely gliding rod without any neighbor is considered as a cluster of size $n = 1$.

We study systems at intermediate densities, where ρ_{rod} is neither very low, such that there are hardly any collisions, nor high enough for a nematic phase to appear for rods in thermal equilibrium, *i.e.* densities lower than the critical density $\rho_c = 3\pi/(2L_{rod}^2)$ of the isotropic-to-nematic phase transition [35].

The statistical quantities, which will be analyzed in Secs. III and IV, are listed in Table I.

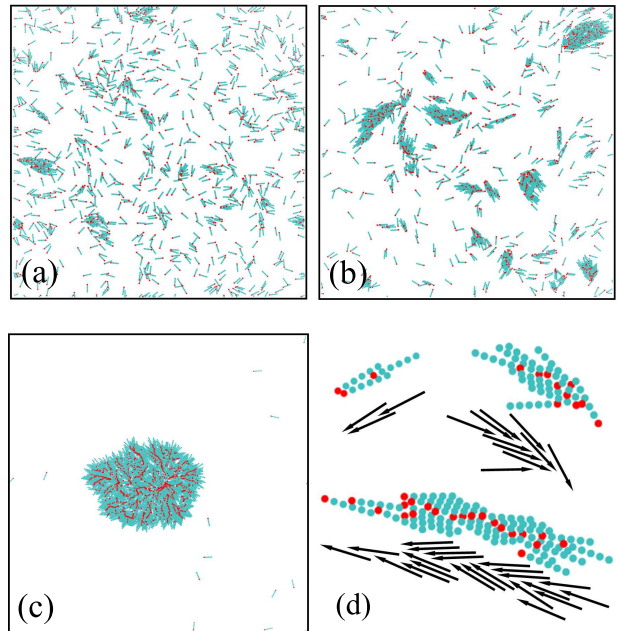


FIG. 2: (Color) Snapshots of the SPR systems at different stationary states. Parameters are $\rho_{rod}L_{rod}^2 = 0.7744$ and (a) $1/\text{Pe} = 0.02645$ (Π_1); (b) $1/\text{Pe} = 0.00501$ (Π_2); (c) $1/\text{Pe} = 0.00041$ (Π_3). Red dots mark the front ends of the rods. (d) Close-up of clusters of size $n = 3, 10$ and 22 shows the partially blocked structure; chosen from a simulation with parameters $\rho_{rod}L_{rod}^2 = 0.7744$ and $1/\text{Pe} = 0.00095$. For a movie see Ref. [53].

A. Cluster-Size Probability Density Functions and Stationary States

For a system with particles distributed at random in space, the probability of finding n particles in some area obeys a binomial distribution; in our SPR systems, the probability to find large particle numbers n is increased by aggregation and clustering. The stationary cluster-size probability density function (PDF) $\Pi(n)$ results from the balance between the cluster formation and break-up rates. While the former depends on the collision rate of clusters, the latter depends also on the environmental noise and the cluster size. We distinguish three different stationary states in our SPR systems by comparing the shapes of their corresponding PDFs. Snapshots are shown in Fig. 2, a movie can be found in Ref. [53].

A disordered state, where rods are distributed in the whole space and oriented in different directions, is characterized by a PDF denoted as Π_1 in Fig. 3. In a snapshot (Fig. 2a), a weak aggregation tendency can be recognized in this case, where several small clusters of well polarized members glide in arbitrary directions. Π_1 decreases as a power law for small cluster sizes, then decays exponentially for large n . The same kind of PDF has also been found in simulations of swarms of point-like SPP interacting via a phenomenological alignment mechanism [11, 16]. The range of the power-law-decay regime of Π_1 depends on the rod density and the environmental noise. Increasing density or decreasing noise shifts the exponential

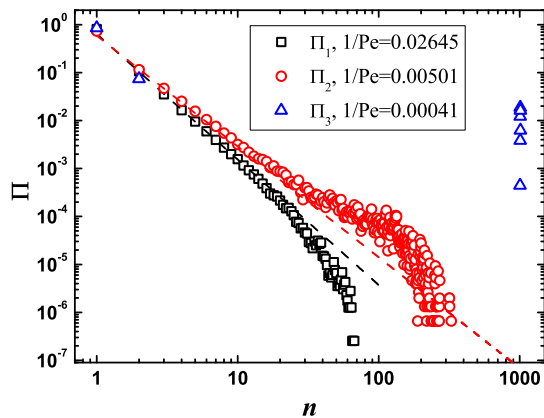


FIG. 3: (Color online) Cluster-size distribution functions $\Pi(n)$ for systems shown in the snapshots of Fig. 2(a), Π_1 (\square , black), Fig. 2(b), Π_2 (\circ , red), and Fig. 2(c), Π_3 (\triangle , blue).

cut-off to larger n .

The system with the second type of PDF, denoted Π_2 in Fig. 3, is more ordered, with an obvious tendency to form large clusters. A snapshot (Fig. 2b) shows several large and motile clusters moving in different directions. Π_2 also displays a power-law decay at small cluster sizes, but shows an increased probability (compared to the power-law decay) of finding large clusters. Increasing the number density or decreasing the noise shifts the prominent shoulder to larger cluster sizes. For very large aggregates, greater than the shoulder location, Π_2 decreases rapidly.

The system with the third type of PDF, denoted Π_3 in Fig. 3, is characterized by a giant cluster, in which most rods are oriented radially towards the center (Fig. 2c). The giant cluster forms when several smaller motile clusters collide head-on in a short time interval, such that a nucleus with a blocked structure emerges. This nucleus continues to grow until most of rods in the system are gathered in it. Π_3 has two parts, a peak at large n representing the giant clusters, and another peak at very small n corresponding to some freely swimming rods not collected by the giant cluster. The average rod density outside the giant clusters is very low.

Both Π_1 and Π_2 display a power-law decay at small cluster sizes,

$$\Pi \sim n^\beta. \quad (17)$$

The exponent β is a function of the rod density ρ_{rod} and noise $1/Pe$; it increases with increasing ρ_{rod} and decreases with increasing $1/Pe$ (Fig. 4). However, the dependence of β on ρ_{rod} or $1/Pe$ in the Π_1 regime is much stronger than in the Π_2 regime; in the latter case, β approaches -2 .

By systematically varying the rod density ρ_{rod} and the environmental noise level, we can construct a phase diagram with regions characterized by different types of PDFs, see Fig. 5. Clearly, Π_1 is found in the low-density and high-noise regime, Π_3 in the high-density and low-noise regime, and Π_2 is associated with the transition region between Π_1 and Π_3 . Note that all systems in Fig. 5 were started from disordered initial states.

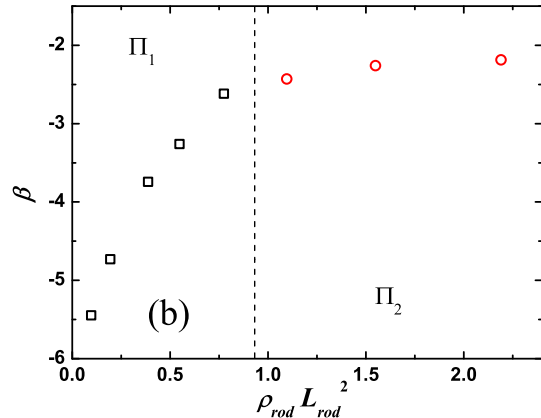
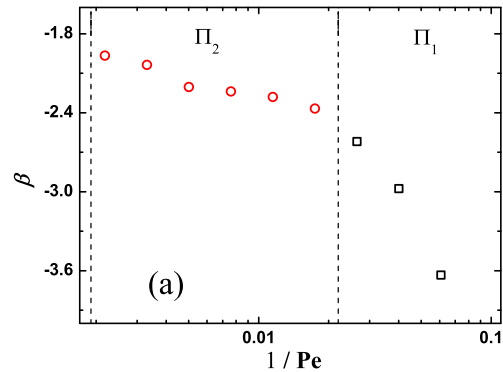


FIG. 4: The exponent β of the power-law part of Π_1 and Π_2 as a function of (a) the environmental noise $1/Pe$ when $\rho_{rod}L_{rod}^2 = 0.7744$, and (b) the rod density $\rho_{rod}L_{rod}^2$ when $1/Pe = 0.02645$.

Systems characterized by the probability density function Π_2 bear some similarity with liquid systems supercooled below the freezing point. Note the system with $1/Pe = 0.00095$ and $\rho_{rod}L_{rod}^2 = 0.7744$ in Fig. 5 displays both Π_2 and Π_3 distributions corresponding to simulations with different initial random states. Systems with the probability density function Π_3 show the characteristics of a glassy behavior, where the dense packing of rods arises from the random collisions, and remains frozen at later times.

Our results are consistent with those of Ref. [37]. By comparing short runs for systems with and without fluctuations, the transition from Π_1 to Π_2 was found in Ref. [37] to shift to larger values of the aspect ratio L_{rod}/l_b and total area fraction of rods $\eta = \rho_{rod}L_{rod}l_b$. Fig. 5 demonstrates that in our system the transition shifts with increasing $1/Pe$ to larger $\rho_{rod}L_{rod}^2$, which is proportional to $\eta L_{rod}/l_b$.

B. Orientational Correlation Functions

Although we distinguish three swarming states in our SPR systems, there are only two types of cluster structures. The motile clusters in the Π_1 and Π_2 states consist of polarized

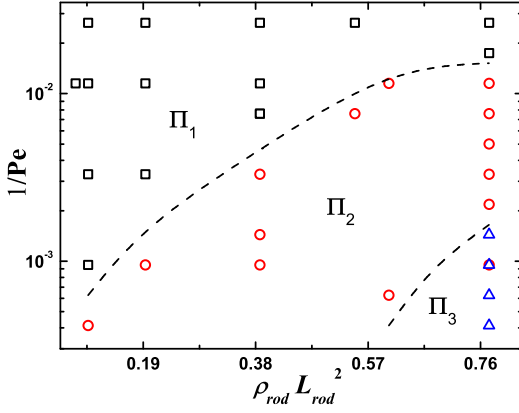


FIG. 5: (Color online) Dynamical phase diagram of swarm behavior. Symbols indicate systems with PDF Π_1 (\square , black), Π_2 (\circ , red) and Π_3 (\triangle , blue). All systems were started from a random initial state. The dashed lines are guides to the eye.

rods, as shown in Fig. 2a,b. In contrast, the giant clusters found in the Π_3 state consist of a large number of rods blocking each other in their forward motion, as shown in Fig. 2c.

These two types of clusters can be distinguished by analyzing the orientational correlation function

$$G(\mathbf{r}) = \frac{1}{N_{rod}(N_{rod} - 1)} \sum_i \sum_{j \neq i} \langle \hat{\mathbf{u}}_i \cdot \hat{\mathbf{u}}_j \cdot \delta(\mathbf{r} - \mathbf{r}_{ij}) \rangle. \quad (18)$$

Here $\hat{\mathbf{u}}_i$ is the unit vector denoting the orientation of rod i , $\mathbf{r}_{ij}(r, \phi)$ is the vector pointing from the center of mass of rod i to rod j , and ϕ is the angle between $\hat{\mathbf{u}}_i$ and \mathbf{r}_{ij} . $G(r) \rightarrow 1$ for $r \rightarrow 0$ because two neighboring rods at close distance are always aligned. At large distance, $G(r) \rightarrow 0$.

When the system is in a state characterized by Π_1 or Π_2 , $G(\mathbf{r})$ is symmetric with respect to the direction $\phi = 0^\circ$ with a maximum at $r = 0$ (Fig. 6a). The slight elongation of $G(\mathbf{r})$ in the directions $\phi = 0^\circ$ and $\phi = 180^\circ$ indicates that the clusters tend to slightly extend in the direction of the average rod orientation due to packaging. The width of $G(\mathbf{r})$ is narrower in the front and wider in the back, because of their partially blocked structure (see Fig. 2d) and because large clusters are more likely to collide with other clusters head-on. If an head-to-head collision does not result in the formation a larger cluster or a blocked structure, the front tips are sharpened due to the ‘‘attrition’’ of the two clusters.

If the system is in the state with a giant cluster, $G(\mathbf{r})$ shows a very different behavior, see Fig. 6b. $G(\mathbf{r})$ still has a positive maximum near $r = 0$, which represents a high local orientational order. However, a region with negative correlations, $G < 0$, develops, with a minimum at some (r', ϕ') . Because all rods point preferentially towards the center of cluster, the propelling forces of the rod nearly compensate each other. Therefore, the locomotion speed of a giant cluster is much smaller than the gliding speed of a single rod. Moreover, the propelling forces generate a net torque due to the deviation of the rod orientations from pointing exactly towards the center of mass, which implies a rotational motion of the giant cluster.

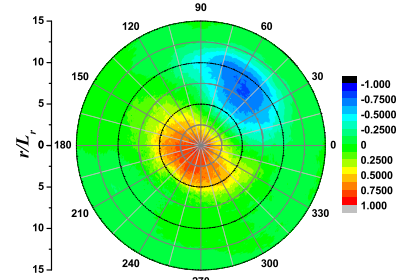
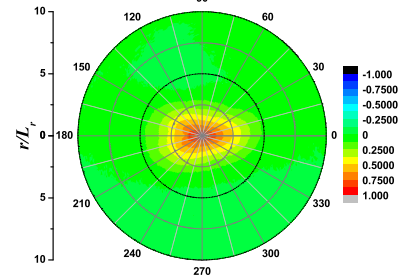


FIG. 6: (Color) The orientational correlation function $G(\mathbf{r})$ as a function of the relative position \mathbf{r} (a) in a system with Π_2 ($\rho_{rod}L_{rod}^2 = 0.7744$ and $1/Pe = 0.00501$), where there are motile clusters; (b) in a system with Π_3 ($\rho_{rod}L_{rod}^2 = 0.7744$ and $1/Pe = 0.00041$) characterized by the presence of a giant cluster.

ϕ' is related to this rotation. For $0^\circ < \phi' < 90^\circ$, the cluster rotates counterclockwise; for $-90^\circ < \phi' < 0^\circ$, it rotates clockwise; for $\phi' = 0^\circ$, there is no net torque and the giant cluster does not rotate.

C. Average Cluster Size

The average cluster size $\langle n \rangle$ of the system is

$$\langle n \rangle = \sum_n n \Pi(n), \quad (19)$$

where $\Pi(n)$ is the normalized cluster-size distribution function. $\langle n \rangle$ increases with increasing ρ_{rod} , as shown in Fig. 7a; in the low-density limit, $\langle n \rangle$ approaches unity. $\langle n \rangle$ decreases with increasing noise level, $1/Pe$, as shown in Fig. 7b. In the Π_2 regime, the system exists in two metastable states, depending on the initial conditions. With random initial conditions, a ‘‘supercooled’’ state emerges, which transforms into the Π_3 state once a giant-cluster nucleus has formed. This can be seen in Fig. 7b for $1/Pe = 0.00095$, where two data points show simulation results with different random number for random initial states. With a giant cluster as initial state, the system

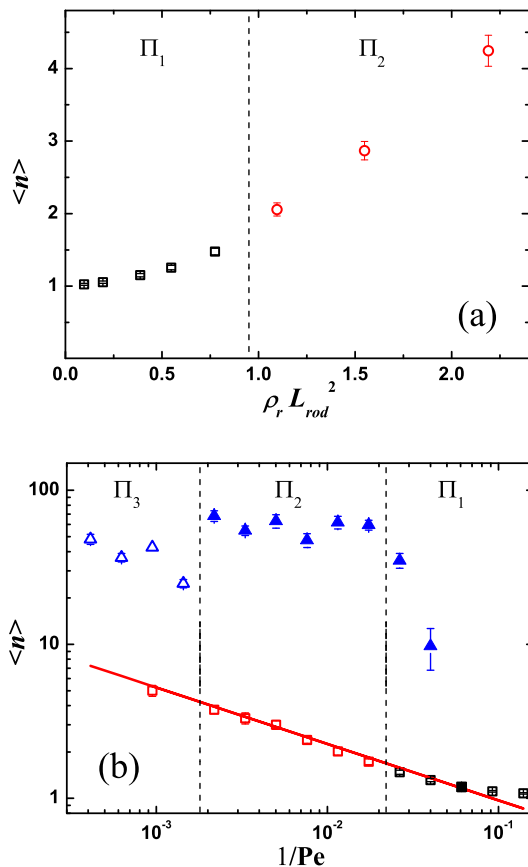


FIG. 7: (Color online) The average cluster size $\langle n \rangle$ as a function of (a) the rod density $\rho_{rod} L_{rod}^2$ with $1/Pe = 0.02645$ and (b) the environmental noise $1/Pe$ with $\rho_{rod} L_{rod}^2 = 0.7744$. The solid (red) line is a fit of the power-law part with exponent $\zeta = 0.37$. The dashed (black) lines are the boundaries separating different regions in the phase diagram (Fig. 5). The open symbols represent systems with Π_3 (Δ , blue), Π_2 (\circ , red), and Π_1 (\square , black), starting from random initial states. The solid symbols represent the systems with Π_2 (\blacktriangle , blue) and Π_1 (\blacksquare , black), starting from a state with a giant cluster.

stays in the Π_3 state unless the noise is large enough to destroy the giant cluster; this occurs in Fig. 7b for $1/Pe = 0.04$. Interestingly, $\langle n \rangle$ shows a power-law decay

$$\langle n \rangle \sim Pe^\zeta \quad (20)$$

in the Π_1 and Π_2 region when the system starts from a disordered state, with exponent $\zeta \simeq 0.37$.

D. Cluster Lifetime

We define the lifetime of a cluster as the length of the time during which its members do not change. The lifetime of a cluster is analyzed with a time interval $\Delta\tau = 100$; thus, cluster lifetimes less than $\Delta\tau$ cannot be resolved. The average cluster lifetime T_{life} is a function of cluster size n .

As shown in Fig. 8, the lifetimes of the clusters of size $n = 1$ are always much longer than of other cluster sizes, because

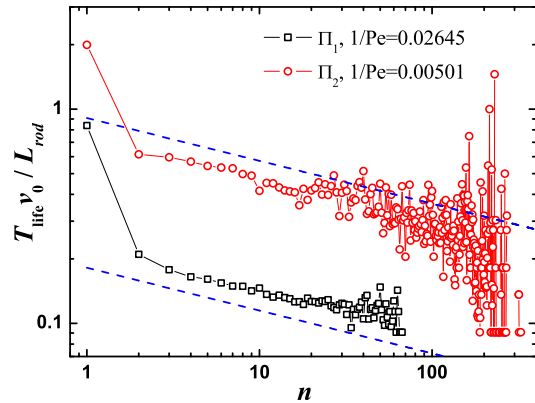


FIG. 8: (Color online) Average cluster lifetime $T_{life}(n)$ for systems with the same rod number density $\rho_{rod} L_{rod}^2 = 0.7744$ but with a different noise level, as indicated. The dashed lines are power laws (21) with an exponent $\delta = 0.2$.

single-rods “clusters” cannot disintegrate. For $n \geq 2$, $T_{life}(n)$ decreases smoothly with increasing cluster size. The data for mid-size clusters ($2 < n < 30$) show an effective power-law dependence,

$$T_{life}(n) \sim n^{-\delta} \quad (21)$$

with an exponent $\delta \simeq 0.2$. Because the environmental noise determines the break-up rate of clusters, T_{life} increases with decreasing $1/Pe$. We only show the lifetime of motile clusters in systems characterized by Π_1 and Π_2 . The giant clusters found in the state characterized by Π_3 can persist for a very long time until a sufficiently large fluctuation occurs.

To understand the dependence of the cluster lifetime on n , we can assume that only single rods are lost at the cluster surface [37]. In this case, the probability to loose a rod per unit time is proportional to the perimeter length, which scales as $n^{1/2}$ (for compact clusters of approximately circular shape). Therefore, this simple argument implies a scaling law (21) with exponent $\delta = 0.5$. The growth of clusters is more complex, since it can occur by collision with all types of other clusters; however, the collision cross-section should again be proportional to $n^{1/2}$. The value of $\delta = 0.5$ is considerable smaller (corresponding to shorter lifetimes for larger clusters) than observed in our simulations. This indicates that there must be another mechanism of cluster decay. Indeed, the typical cluster configurations of Fig. 2d indicate that only at few places along the perimeter, rods may have the possibility to leave the cluster.

E. Finite-Size Effects

In our simulations, the finite simulation-box size implies a finite number of particles. A cluster can never grow larger than the total number of rods in the system. Consequently, all quantities related to the cluster size, such as the cluster size distribution Π and the stationary average cluster size $\langle n \rangle$

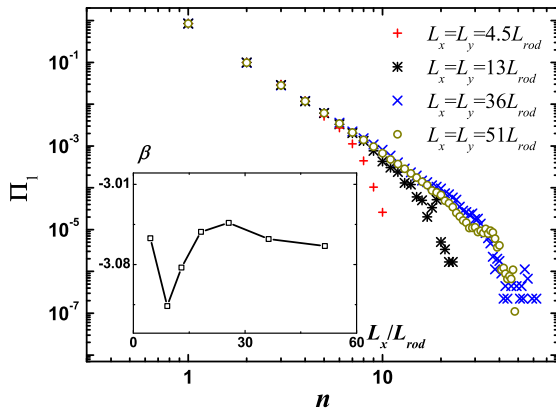


FIG. 9: (Color online) Effect of finite system size on the probability density distribution function $\Pi_1(n)$ for $\rho_{rod}L_{rod}^2 = 0.7744$, $1/Pe = 0.04009$, and different simulation box sizes, as indicated. The inset shows the exponent β of the power-law part of $\Pi_1(n)$ as a function of the size L_x of the simulation box.

display finite-size effects. Similarly, density fluctuations at the scale of the simulation-box size are suppressed.

For the probability density function $\Pi(n)$, the absence of cluster larger than N_{rod} does not only introduce a cut-off at large cluster size, but also affects the exponent β of the power-law part, as shown in Fig. 9. For systems with Π_1 , the data for small box sizes ($L_x = L_y = 4.5L_{rod}$ and $13L_{rod}$) still obey a power-law decay at small n , without an obvious change of the exponent, as shown in the inset of Fig. 9, but they deviate from the power law when n approaches N_{rod} . When the simulation box is large ($L_x = L_y = 36L_{rod}$ and $51L_{rod}$), the PDFs almost coincide, and their exponential cut-offs are observed at the same value of n ; also, β approaches an asymptotic value when L_x increases. Therefore, we conclude that our results for the larger systems represent the thermodynamic limit. Similarly, the power-law part of Π_2 extends with increasing box size, and the location of the prominent shoulder shifts to larger cluster size. The finite-size effects are significantly stronger for systems in the Π_3 region of the phase diagram. When the system is too small, the total rod number is not sufficient to trigger the formation of a blocked structure. The system then stays in a Π_2 state. This supports the claim that the state with Π_2 is a “supercooled” state. We believe that the absence of the Π_3 state in Ref. [37] is due to finite-size effect; a system of only 100 rods is too small to form a blocked structure.

The dependence of the average cluster size $\langle n \rangle$ on the linear system size L_x is shown in Fig. 10. For systems with Π_1 and Π_2 , $\langle n \rangle$ increases with L_x and eventually reaches a plateau value. For the system with Π_3 , $\langle n \rangle$ strongly diverges when L_x increases. Thus, $\langle n \rangle$ can be considered as an intensive quantity in the first two states, and as an extensive quantity in the third state.

Suppose the probability density function $\Pi(n)$ obeys a power law for all cluster sizes,

$$\Pi(n) = \frac{1 + \beta}{N^{1+\beta} - 1} n^\beta, \quad (22)$$

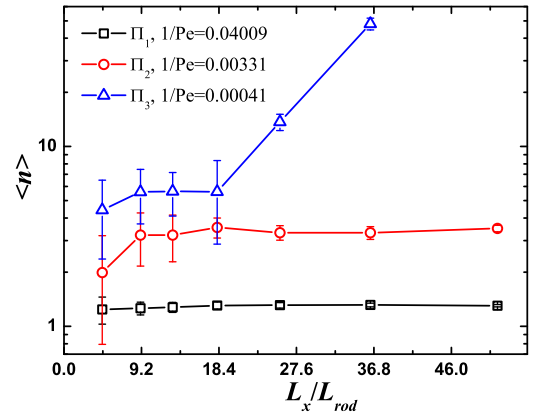


FIG. 10: (Color online) The average cluster size $\langle n \rangle$ as a function of the size L_x of the simulation box for the three clustering states. The number density is $\rho_{rod}L_{rod}^2 = 0.7744$ in all systems.

where $\beta < -1$ and $N = \rho_{rod}L_xL_y$ is the total number of rods in the system. It is easy to verify that for $N \gg 1$, where sums over n can be well approximated by integrals, $\int_1^N \Pi(n)dn = 1$, so that $\Pi(n)$ is properly normalized. The sharp drop due to the limited box size is neglected. In this case, the average cluster size of the system is obtained to be

$$\langle n \rangle = \begin{cases} -(1 + \beta)N^{2+\beta}/(2 + \beta), & -2 < \beta < -1 \\ (1 - N^{-1})^{-1} \ln N, & \beta = -2 \\ (1 + \beta)/(2 + \beta), & \beta < -2 \end{cases} \quad (23)$$

For $-2 < \beta < -1$, the average cluster size strongly depends on the total number N of rods, whereas for $\beta < -2$, $\langle n \rangle$ is independent of N . For large negative β , $\langle n \rangle$ approaches unity, which means that all rods are gliding freely.

In our simulations, the effective exponents in the Π_1 and Π_2 regimes are $-6 \leq \beta \leq -2.5$ and $-2.5 \leq \beta \leq -2.0$, respectively, see Fig. 4. Thus, Eq. (23) implies that finite-size effects are weak in the Π_1 regime, and are pronounced in the Π_2 regime, in agreement with the simulation results of Fig. 10. (Eq. (23) does not apply to the Π_3 state since the assumption of a power-law dependence (22) does not hold.)

IV. SWARMING BEHAVIOR OF FLAGELLA IN A MPC FLUID

Multi-flagellum systems show a similar swarming behavior, consisting of aggregation and clustering, as observed in Sec. III for self-propelled rods (see Fig. 11 and movie [53]). Synchronization of the flagellar beat, and attraction and alignment of flagella do not only arise from volume exclusion, as in the SPR systems, but are also triggered by the hydrodynamic interactions between the sinusoidally undulating bodies [43, 44]. At the same time, hydrodynamic interactions between flagella act as a source of environmental noise, which causes the flagella trajectories to fluctuate strongly.

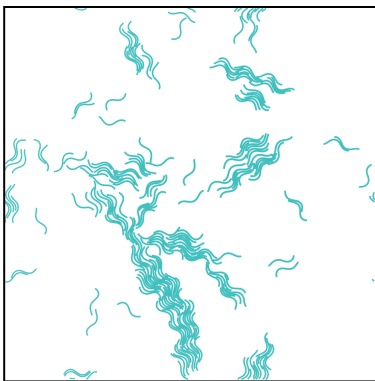


FIG. 11: (Color online) Snapshot of a multi-flagellum system in a MPC fluid. The parameters are $\rho_{fl}L_{fl}^2 = 1.5625$ and $\sigma_{fl} = 0.1\%$. The black box shows the boundary of the simulation box. Periodic boundary conditions are employed. For a movie see Ref. [53].

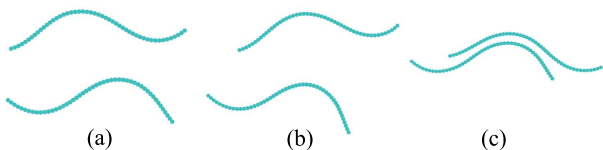


FIG. 12: (Color online) Synchronization and attraction of two flagella. The flagella have the same beating frequency $f = 1/120$, and a phase difference $\Delta\varphi = 0.5\pi$. The snapshots are taken at the times (a) $tf = 0.167$, (b) $tf = 4.17$ and (c) $tf = 22.2$.

A. Hydrodynamic Synchronization, Attraction, and Aggregation

The synchronization and attraction of two flagella is shown in Fig. 12. Synchronization is achieved within about four beats, while the formation of a tight pair from an initial distance of about one-third of the flagellar length takes about 20 beats. The flow field of a flagellum is shown in Fig. 13. The flow field at a certain time in the beating cycle (Fig. 13a) shows that formation of two vortices, which propagate from the front to the rear end as the flagellum moves forward.

The hydrodynamic interaction of swimmers depends on the type of self-propulsion. The average flow field of flagellum, integrated over the whole beating cycle, demonstrates that the flagellum, which might be expected to be a “neutral” swimmer (*i.e.*, neither a pusher nor a puller) is indeed a very weak pusher — where the dominant propulsion is located closer to the rear end — because the line connecting the centers of the two vortices intersects the average flagellum shape behind its mid-point (Fig. 13b). This generates a in-flow from both sides of the flagellum near the front end, which is responsible for hydrodynamic attraction [40, 41].

In multi-flagellum systems, large clusters can form by collisions of smaller clusters, supported by the hydrodynamic attraction between neighboring flagella; large clusters can disintegrate into smaller components due to the diversity of flagellar frequencies, or the hydrodynamic flow fields of other clusters. With hydrodynamic interactions, large clusters of flag-

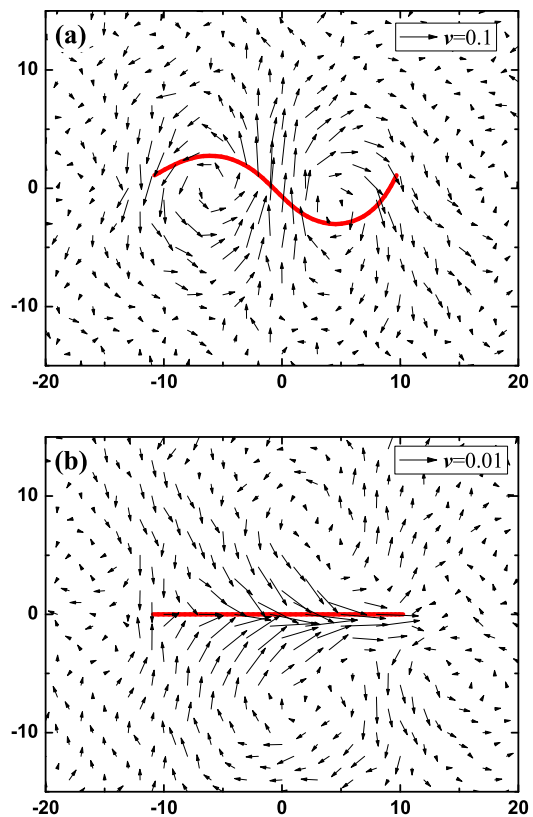


FIG. 13: (Color online) Flow field of a single flagellum, (a) at a fixed time in the beating cycle, and (b) averaged over the whole beating cycle. A snapshot of the flagellum and the average flagellum shape are superimposed in (a) and (b), respectively. The scale bar indicates the magnitude of the flow velocities.

ella are usually strongly extended in their direction of motion, as shown in Fig. 11 and movie [53]. The flagella inside the cluster are well synchronized. This structure is reminiscent of the “sperm-train” structure observed in rodent-sperm experiments [27, 28]. The elongated clusters can extend to distances as large as the side length of the simulation box, which induces strong finite-size effects.

Similar to the definition of a rod cluster in Sec. III, a flagellum cluster is defined as a set of flagella that are connected or neighbors either directly or through other agents at a given moment in time. Its size is the number n of flagella it contains. A freely-swimming single flagellum is considered as a cluster of size $n = 1$.

B. Cluster-Size Distributions

Both probability density functions Π_1 and Π_2 are observed in our multi-flagellum systems, as shown in Fig. 14. The variance σ_{fl} of the distribution of beat frequencies is used as a measure of the noise level. At low ρ_{fl} or high σ_{fl} , we find Π_1 ; at high ρ_{fl} or low σ_{fl} , we observe Π_2 . In contrast to Π_2 for SPR systems in Sec. III A, Π_2 for flagella systems displays a

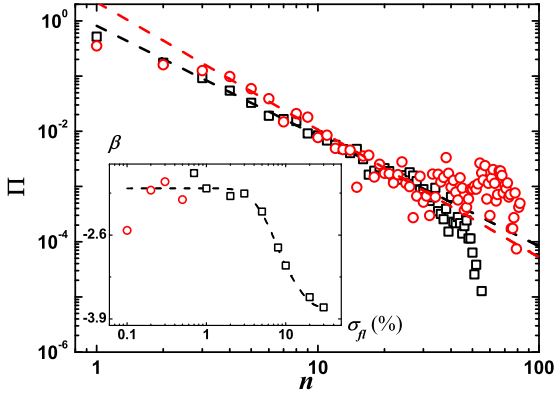


FIG. 14: (Color online) The two different types of cluster-size probability density functions $\Pi_1(n)$ with $\sigma_{fl} = 2\%$ (\square , black), and $\Pi_2(n)$ with $\sigma_{fl} = 0.1\%$ (\circ , red), observed in multi-flagellum systems with density $\rho_{fl}L_{fl}^2 = 1.5625$. The dashed lines are fits to the power-law parts of each PDF. The inset shows the exponent β as a function of the variance σ_{fl} of the frequency distribution. Symbols indicate the systems characterized by Π_2 (\circ , red) and Π_1 (\square , black). The dashed line is a guide to the eye.

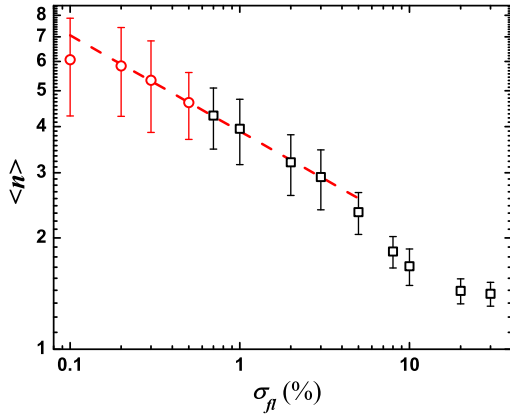


FIG. 15: (Color online) Stationary average cluster size $\langle n \rangle$ versus the variance σ_{fl} of the frequency distribution, for flagellar density $\rho_{fl}L_{fl}^2 = 1.5625$. Symbols indicate systems with Π_1 (\square , black) and Π_2 (\circ , red). The error bars are the standard deviation of the fluctuations. The dashed line indicates a power-law decay with an exponent $\zeta = 0.26$.

deviation from the power-law behavior for very small cluster sizes, $n = 1$ and $n = 2$. We believe that this is due to the hydrodynamic synchronization and attraction of neighboring flagella. For flagella, we have never observed a giant cluster with a blocked structure, in contrast to the SPR system of Fig. 2c.

Although the distribution of beating frequencies is an internal property of the swimmers, the influence of σ_{fl} on the exponent β of Eq. (17) is similar to the influence of the environmental noise in our previous SPR simulations, as shown in the inset of Fig. 14. β is nearly constant for $\sigma_{fl} < 3\%$, then decreases smoothly with increasing σ_{fl} .

The average cluster size $\langle n \rangle$ in the stationary state is a func-

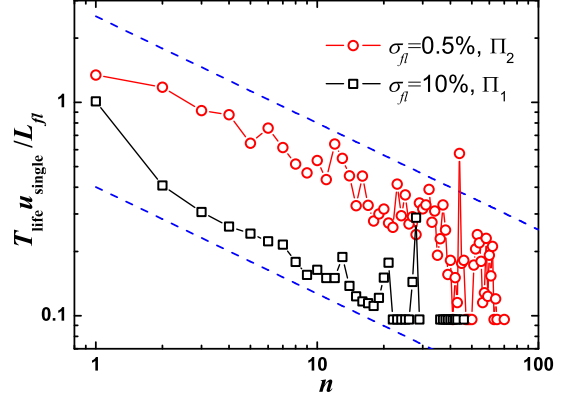


FIG. 16: (Color online) The lifetime $T_{life}^{v, single} / L_{fl}$ of flagella clusters versus their size n . The flagella number density is $\rho_{fl}L_{fl}^2 = 1.5625$. The dashed lines indicate a power law with exponent $\delta = 0.5$.

tion of σ_{fl} , as shown in Fig. 15. Increasing σ_{fl} results in an increase of the overall break-up rate; hence $\langle n \rangle$ decreases. In the large σ_{fl} limit, $\langle n \rangle$ approaches unity, corresponding to a disordered state with randomly distributed flagella. The power-law decay

$$\langle n \rangle \sim \sigma_{fl}^{-\zeta} \quad (24)$$

of the average cluster size with exponent $\zeta \simeq 0.26$ emphasizes the universality of the swarming behavior of rSPP systems in two dimensions. The power-law scaling of $\langle n \rangle$ as a function of σ_{fl} implies a divergence when $\sigma_{fl} \rightarrow 0$. We believe that the small deviation from the power-law behavior for $\sigma_{fl} = 0.1\%$ in Fig. 15, as well as the deviation of β from the plateau value for $\sigma_{fl} = 0.1\%$ in Fig. 14, are due to finite-size effects.

C. Cluster Lifetimes

The average cluster lifetime $T_{life}(n)$ decreases as an effective power-law function of cluster size n , see Eq. (21), with an exponent $\delta \simeq 0.5$, as shown in Fig. 16. The value of δ is very close to the prediction based on the assumption of a mechanism of particle accumulation and shedding proportional to the cluster perimeter, as presented in Sec. III D. This good agreement provides further evidence for the different mechanisms of cluster stabilization for rods and flagella, which are a (partially) blocked motion and a hydrodynamic attraction, respectively.

Note that the system size of the flagella simulations is not as large as for the SPR systems. Thus, the effective power law can only be observed over a smaller range of cluster sizes. In SPR simulations, single rods ($n = 1$) always have a much longer lifetime compared to expectation from the effective power law, see Fig. 8. In contrast, for flagella with full hydrodynamic interactions, $T_{life}(1)$ is much closer to the power-law extrapolation, and can even be lower than the power-law prediction (e.g. for $\sigma_{fl} = 0.5\%$ in Fig. 16).

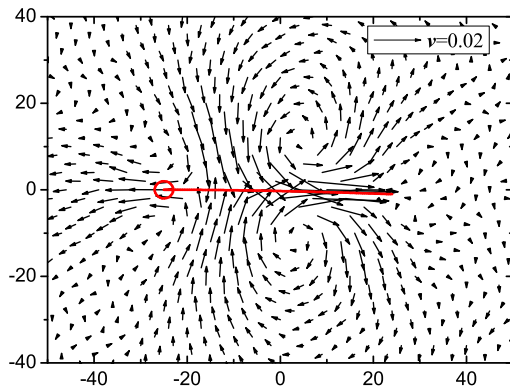


FIG. 17: (Color online) Flow field of a single sperm, beating with two sine waves on its tail, averaged over the whole beating cycle. The average sperm shape is superimposed. The scale bar indicates the magnitude of the flow velocities.

D. Comparison of Sperm and Flagella

As explained in Sec. II B, our model of a flagellum differs from the model of a sperm employed in Ref. [43] by the absence of a passive midpiece and a circular head. Also, in the sperm simulations [43], two sine waves were present on the tail, while a single sine wave is present on the flagellum.

How similar or different is the collective behavior of sperm and flagella? There are three different aspects to this question. *Synchronisation* depends mainly on the interaction of the time-dependent oscillatory flow field of two neighboring flagella [24, 44], and is therefore very similar, as can be seen from the results presented in Sec. IV A and those of Ref. [43]. On the other hand, the *hydrodynamic attraction* of sperm and flagella is quite different. A sperm cell, consisting of a flagellum and a large head, is clearly a pusher, as demonstrated by the average flow field of a sperm in Fig. 17. The flagellum pushes the fluid backward in both cases, but the bulky head of the sperm drags the fluid forward much more strongly, which generates the characteristic sidewise inflow of fluid towards the midpiece region [40, 41, 45]. In contrast, flagella are very weak pushers, as demonstrated in Fig. 13b above. Therefore, sperm have stronger hydrodynamic attraction than flagella.

Finally, the *swarming behavior* in both flagella and sperm system is characterized by cluster-size distributions and the dependence of the average cluster size on the width σ_{fl} of the distribution of beat frequencies. While the cluster-size distribution of flagella follows a power-law decay over a wide range, it was not possible to clearly identify a power-law behavior for sperm in Ref. [43] due to the relatively small systems of 25 and 50 sperm. The average cluster size is found to depend on σ_{fl} as $\langle n \rangle \sim \sigma_{fl}^{-\zeta}$, with $\zeta = 0.20$ for sperm [43] and $\zeta = 0.26$ for flagella. Larger systems have to be investigated to see whether the exponents ζ for sperm and flagella are different or not. In any case, the stronger hydrodynamic attraction of sperm, which favors larger cluster sizes, is partially offset by the bulky head of sperm, which implies that the sperm clusters in Ref. [43] are much more loosely packed

than the flagella clusters studied here.

V. SUMMARY AND CONCLUSIONS

We have simulated systems of rigid rods propelled by a constant force along their long axis, and systems of flagella propelled by a sinusoidal beating motion, in two dimensions. In both systems, we observe cluster formation and break-up, controlled by the particle density and the internal or external noise. In our simulations, the particle density is always much lower than the critical density of a nematic phase in thermal equilibrium.

Without any attractive potential, self-propelled rods (SPR) exhibit an aggregation behavior triggered only by volume exclusion. Three characteristic types of cluster-size probability density functions $\Pi(n)$ appear in different regions of a dynamic phase diagram of stationary states. At high noise and low density, the system is characterized by Π_1 , which shows a power-law distribution over a range of cluster sizes, with an exponential cutoff at large cluster sizes. At low noise and high density, the system is in a state characterized by Π_3 , which has a peak at sizes near the total number of particles in the system, representing a giant cluster. Systems in an intermediate region of noise and density are characterized by Π_2 , which is a transition state between Π_1 and Π_3 . It has a bimodal shape, with a power-law decay at small cluster sizes and a shoulder at larger sizes. Clusters in Π_1 and Π_2 systems retain a high motility, whereas the giant clusters found in the third state is almost immobile due to its blocked configuration. The average cluster size at equilibrium, directly related to cluster-size distribution Π , displays a power-law dependence with decreasing noise amplitude before the system reaches the Π_3 state.

Sinusoidally beating flagella were simulated in a low-Reynolds-number fluid with full hydrodynamics as an example of self-propelled rod-like particles with explicit propulsion mechanism. Flagella synchronize their beats and attract each other through the hydrodynamic interactions. Despite the different propulsion mechanisms, the basic swarm behavior of aggregation and clustering observed for swimming flagella is remarkably similar to the behavior seen in SPR systems. We observe both Π_1 and Π_2 cluster-size probability density functions by varying the width σ_{fl} of the flagellar beat-frequency distribution, which acts as a source of internal noise in the system. The average cluster size also display a power-law dependence on σ_{fl} , as for SPR systems.

Despite these similarities in the clustering behavior, the two systems show some important differences. They can be traced back to the hydrodynamic attraction between beating flagella, which is absent in our simulations of self-propelled rods. First, the configurations of the flagella clusters consist of tightly stacked flagella with synchronized shapes, and extend in their moving directions. Those elongated clusters are reminiscent of the huge, mobile “sperm trains” observed in rodent-sperm experiments [27]. Clusters in the SPR systems are more compact, and have a wedge-like structure, which arises from the partially blocked rod motion responsible for the cluster aggregation, as well as from collisions with other

clusters. Second, the Π_3 state of a completely blocked structure, which is observed for SPR at high density and low noise, does not seem to exist in flagellar systems. Third, the cluster lifetimes decay with different effective power laws, $\delta = 0.2$ for SPR and $\delta = 0.5$ for flagella. Finally, hydrodynamic interactions between different flagella clusters act as an additional source of noise and contribute to increase the break-up rate.

The existence of the giant, immobile cluster should depend sensitively on the aspect ratio and the type and range of the interactions between self-propelled rods, where longer rods and shorter-range interaction favors the giant-cluster formation. This conclusion follows from the result of Ref. [37] for rods of aspect ratio $L_{rod}/l_b \leq 12$ that Π_1 - Π_2 boundary shifts to higher density with decreasing rod length, and our result of Fig. 7 that the Π_2 state corresponds to “supercooled” liquid state which transforms into the Π_3 state once a giant-cluster nucleus has formed. Blocked clusters were not seen in Ref. [37] for rod lengths $L_{rod}/l_b \leq 12$ due to the relatively small system size with $N_{rod} = 100$. However, blocked states were observed in Ref. [36] for a much larger rod length, $L_{rod}/l_b = 40$, already for a system of only about 50 rods at density $\rho_{rod}L_{rod}^2 = 2$.

Our simulations have been restricted to the isotropic phase

of rods in thermal equilibrium. It will be interesting to see in the future whether immobile, blocked states can also exist (or even dominate) in the nematic regime, or whether they are suppressed by the preferred rod orientation.

In the light of our results, we conclude that different systems of rod-like self-propelled particles display a universal swarming behavior, but also specific properties related to their propulsion mechanisms and the presence or absence of hydrodynamic interactions.

Acknowledgments

We thank Jens Elgeti and Roland Winkler for stimulating discussions. Yingzi Yang acknowledges support by the International Helmholtz Research School on Biophysics and Soft Matter (IHRS BioSoft). Vincent Marceau is grateful to the RISE program of the DAAD (Germany) and to NSERC (Canada) for financial support. This work was supported in part by the VW foundation through the program “Computational Soft Matter and Biophysics”.

-
- [1] T. Vicsek, A. Czirók, E. Ben-Jacob, I. Cohen and O. Shochet, *Phys. Rev. Lett.* **75**, 1226 (1995).
 - [2] J. Toner and Y. Tu, *Phys. Rev. Lett.* **75**, 4326 (1995).
 - [3] R. A. Simha and S. Ramaswamy, *Phys. Rev. Lett.* **89**, 058101 (2002).
 - [4] S. Ramaswamy, R. A. Simha and J. Toner, *Europhys. Lett.* **62**, 196 (2003).
 - [5] F. Peruani, A. Deutsch, and M. Bär, *Eur. Phys. J. Special Topics* **157**, 111 (2008).
 - [6] A. Baskaran and M. C. Marchetti, *Phys. Rev. Lett.* **101**, 268101 (2008).
 - [7] A. Baskaran and M. C. Marchetti, *Phys. Rev. E* **77**, 011920 (2008).
 - [8] E. Bertin, M. Droz and G. Grégoire, *J. Phys. A: Math. Theor.* **42**, 445001 (2009).
 - [9] B. Szabó et al., *Phys. Rev. E* **74**, 061908 (2006).
 - [10] G. Grégoire and H. Chaté, *Phys. Rev. Lett.* **92**, 025702 (2004).
 - [11] C. Huepe and M. Aldana, *Phys. Rev. Lett.* **92**, 168701 (2004).
 - [12] M. R. D’Orsogna, Y. L. Chuang, A. L. Bertozzi and L. S. Chayes, *Phys. Rev. Lett.* **96**, 104302 (2006).
 - [13] M. Aldana, V. Dosssetti, C. Huepe, V. M. Kenkre and H. Larralde, *Phys. Rev. Lett.* **98**, 095702 (2007).
 - [14] H. Chaté, F. Ginelli, G. Grégoire and F. Raynaud, *Phys. Rev. E* **77**, 046113 (2008).
 - [15] F. Ginelli, F. Peruani, M. Bär, and H. Chaté, *Phys. Rev. Lett.* **104**, 184502 (2010).
 - [16] C. Huepe and M. Aldana, *Physica A* **387**, 2809 (2008).
 - [17] X.-L. Wu and A. Libchaber, *Phys. Rev. Lett.* **84**, 3017 (2000); X.-L. Wu and A. Libchaber, *Phys. Rev. Lett.* **86**, 557 (2001); G. Grégoire, H. Chaté and Y.-H. Tu, *Phys. Rev. Lett.* **86**, 556 (2001).
 - [18] C. Dombrowski, L. Cisneros, S. Chatkaew, R. E. Goldstein and J. O. Kessler, *Phys. Rev. Lett.* **93**, 098103 (2004).
 - [19] A. Sokolov, I. S. Aranson, J. O. Kessler and R. E. Goldstein, *Phys. Rev. Lett.* **98**, 158102 (2007).
 - [20] E. Ben-Jacob, I. Cohen and H. Levine, *Advances in Physics* **49**, 395 (2000).
 - [21] J. M. Kuner and D. Kaiser, *J. Bacteriol.* **151**, 458 (1982).
 - [22] O. A. Igoshin, R. Welch, D. Kaiser and G. Oster, *Proc. Natl. Acad. Sci. U.S.A.* **101**, 4256 (2004).
 - [23] M. S. Alber, M. A. Kiskowski and Y. Jiang, *Phys. Rev. Lett.* **93**, 068102 (2004).
 - [24] G. Taylor, *Proc. Roy. Soc. Ser. A.* **209**, 447 (1951).
 - [25] J. Gray, *J. Exp. Biol.* **35**, 96 (1958).
 - [26] J. Gray and H. W. Lissmann, *J. Exp. Biol.* **41**, 135 (1964).
 - [27] H. D. M. Moore, K. Dvořáková, N. Jenkins and W. G. Breed, *Nature* **418**, 174 (2002).
 - [28] S. Immler, H. D. M. Moore, W. G. Breed and T. R. Birkhead, *PLoS ONE* **1**, e170 (2007).
 - [29] I. H. Riedel, K. Kruse, and J. Howard, *Science* **309**, 300 (2005).
 - [30] W. F. Paxton, et al., *J. Am. Chem. Soc.* **126**, 13424 (2004).
 - [31] Y. Hong, N. M. K. Blackman, N. D. Kopp, A. Sen and D. Velegol, *Phys. Rev. Lett.* **99**, 178103 (2007).
 - [32] V. Narayan, S. Ramaswamy and N. Menon, *Science* **317**, 105 (2007).
 - [33] A. Kudrolli, G. Lumay, D. Volfson and L. S. Tsimring, *Phys. Rev. Lett.* **100**, 058001 (2008).
 - [34] L. Rothschild, *Nature* **198**, 1221 (1963).
 - [35] R. F. Kayser and H. J. Raveché, *Phys. Rev. A* **17**, 2067 (1978).
 - [36] P. Kraikivski, R. Lipowsky and J. Kierfeld, *Phys. Rev. Lett.* **96**, 258103 (2006).
 - [37] F. Peruani, A. Deutsch and M. Bär, *Phys. Rev. E* **74**, 030904(R) (2006).
 - [38] J. Elgeti and G. Gompper, *EPL* **85**, 38002 (2009).
 - [39] H. H. Wensink and H. Löwen, *Phys. Rev. E* **78**, 031409 (2008).
 - [40] E. Lauga and T. R. Powers, *Rep. Prog. Phys.* **72**, 096601 (2009).
 - [41] T. Ishikawa, *J. R. Soc. Interface* **6**, 815 (2009).
 - [42] D. Saintillan and M. J. Shelley, *Phys. Rev. Lett.* **99**, 058102 (2007).
 - [43] Y. Yang, J. Elgeti and G. Gompper, *Phys. Rev. E* **78**, 061903

- (2008).
- [44] G. J. Elfring and E. Lauga, Phys. Rev. Lett. **103**, 088101 (2009).
- [45] J. Elgeti, U. B. Kaupp, and G. Gompper, Biophys. J. **99**, in press (2010).
- [46] R. Kapral, Adv. Chem. Phys. **140**, 89 (2008).
- [47] G. Gompper, T. Ihle, D. M. Kroll and R. G. Winkler, Adv. Polym. Sci. **221**, 1 (2009).
- [48] M. Ripoll, K. Mussawisade, R. G. Winkler and G. Gompper, Europhys. Lett. **68**, 106 (2004).
- [49] I. H. Riedel-Kruse, A. Hilfinger, J. Howard and F. Jülicher, HFSP **1**, 192 (2007).
- [50] T. Ihle and D. M. Kroll, Phys. Rev. E **63**, 020201(R) (2001).
- [51] N. Kikuchi, C. M. Pooley, J. F. Ryder and J. M. Yeomans, J. Chem. Phys. **119**, 6388 (2003).
- [52] T. Ihle and D. M. Kroll, Phys. Rev. E **67**, 066706 (2003).
- [53] See EPAPS Document No. [number will be inserted by publisher] for movies of the clustering and aggregation of self-propelled rods and swimming flagella. For more information on EPAPS, see <http://www.aip.org/pubservs/epaps.html>.